Article

Journal of the Brazilian Chemical Society

https://dx.doi.org/10.21577/0103-5053.20230133

J. Braz. Chem. Soc. **2024**, *35*, 3, e-20230133, 1-16
©2024 Sociedade Brasileira de Química

Performance Study of Ni/Si-MCM-41 Catalysts, Synthesized with Different Silica Sources, and Their Application on Methane Dry Reform to Produce Green Hydrogen

Bárbara B. Cazula, [*,a,b,c] ***Renata O. da Fonseca,*** [d] ***André Luiz A. Marinho,*** [d] ***Fábio B. Noronha,*** [d] ***Pedro Augusto Arroyo,*** [e] ***Carlos I. Yamamoto,*** [f] ***Rodrigo Brackmann*** [g] ***and Helton José Alves*** [a,b]

[a]*Programa de Pós-Graduação em Engenharia de Energia na Agricultura, Universidade Estadual do Oeste do Paraná (Unioeste), R. Universitária, 1619, Universitário, 85819-110 Cascavel-PR, Brazil*

[b]*Laboratório de Materiais e Energias Renováveis (LABMATER), Universidade Federal do Paraná (UFPR), Setor Palotina, R. Pioneiro, 2153, Dallas, 85950-000 Palotina-PR, Brazil*

[c]*Programa de Pós-Graduação em Química, Universidade Estadual de Maringá (UEM), Av. Colombo, 5790, Jardim Universitário, 87020-900 Maringá-PR, Brazil*

[d]*Instituto Nacional de Tecnologia (INT), Av. Venezuela, 82, Praça Mauá, 20081-312 Rio de Janeiro-RJ, Brazil*

[e]*Departamento de Engenharia Química (DEQ), Universidade Estadual de Maringá (UEM), Av. Colombo, 5790, Jardim Universitário, 87020-900 Maringá-PR, Brazil*

[f]*Laboratório de Análises de Combustíveis Automotivos (Lacaut), Centro Politécnico, Universidade Federal do Paraná (UFPR), Av. Cel. Francisco H. dos Santos, 100, Jardim das Américas, 81530-000 Curitiba-PR, Brazil*

[g]*Departamento de Química, Universidade Federal Tecnológica do Paraná (UTFPR), Campus Pato Branco, Via do Conhecimento, Km 1, 85503-390 Pato Branco-PR, Brazil*

The present work carried out an extensive and deepened study regarding the physico-chemical characteristics of two Si-MCM-41-type supports, synthesized employing two distinct silica precursors, tetraethyl orthosilicate (TEOS) and rice husk ash (RHS), with the dispersion of nickel on the surface of the catalytic support. The direct influence of the active phase dispersion was analyzed, making a relationship with the formation of coke and with its performance on methane dry reform (DRM). The catalysts were prepared with 5, 10, and 20% (m/m) of Ni by wet impregnation method (with excess solvent), calcined at 800 ºC for 6 h, and characterized by the techniques of scanning electron microscopy and energy dispersive spectroscopy (SEM/EDS), transmission electron microscopy (TEM), Brunauer-Emmett-Teller (BET)/Barret-Joyer-Halenda (BJH), X-ray diffraction (XRD), Fourier transform infrared spectroscopy (FTIR), temperature-programmed ammonia desorption (TPD-NH_3), and H_2-temperature-programmed reduction (TPR). The DRM experiments were carried out at 800 °C for 24 h with a 1:1 CH_4:CO_2 molar ratio. Analyzes of gaseous products were performed in gas chromatography (GC) and the coke produced was estimated by temperature-programmed oxidation (TPO). The best reaction results were obtained for catalysts with 20% nickel, which were selective and stable within 24 h of reaction. Comparing the TEOS and RHS catalysts for 20% Ni, the DRM results were very similar. The catalysts on RHS support demonstrated a significant low formation of coke, which can be considered negligible in a 24 h reaction.

Keywords: Si-MCM-41, nickel catalysts, green hydrogen, renewable energy, methane dry reforming

*e-mail: barbarabulhoes@hotmail.com
Editor handled this article: Célia M. Ronconi (Associate)

This is an open-access article distributed under the terms of the Creative Commons Attribution License.

Introduction

Synthesis gas is a gaseous mixture composed of hydrogen (H_2) and carbon monoxide (CO),[1] which serves several industrial sectors such as an input for the production of synthetic fuels, solvents, and chemical reagents with high added value[2] by using technologies such as Fischer-Tropsch synthesis for the production of alkanes, alkenes, and alcohols.[3] On an industrial scale, it is produced from non-renewable raw materials, rich in hydrocarbons, such as coal and natural gas, through the methods of gasification and catalytic reforming, respectively.[1] The synthesis gas can also be produced by gasification of biomass and catalytic reforming of biofuels, as is the case of biogas from urban or agro-industrial waste.[4,5] In this context, the hydrogen produced can be considered as "green", since it has zero CO_2 emissions balance, besides being renewable.[6] The purity of the synthesis gas and the H_2/CO ratio found are decisive in choosing the most promising routes for the synthesis of the desired products. Therefore, the types of raw materials, the selected catalysts, and the experimental conditions employed, directly affect the results.[7]

Besides being a renewable alternative to replace natural gas obtained from fossil sources, synthesis gas is a potentially promising and versatile source for obtaining gaseous hydrogen on a large scale.[8] Thus, green hydrogen is an excellent agent in the diversification of the global energy matrix, being able to act in the decarbonization of various industrial sectors and collaborate in critical energy scenarios, standing out as one of the few sustainable alternatives for long-term energy storage.[9] However, according to data made available by the International Energy Agency (IEA),[10] much of the hydrogen is still produced from fossils, accounting for 6% of the global use of natural gas.[11]

Therefore, it is necessary to invest in alternatives that enable the production of hydrogen through renewable routes and that make it possible for its insertion in a larger portion of the world energy scenario.[12] The increasing of the production scale, reduction of the costs of generation technologies, development of an effective and safe storage system, the improvement in hydrogen production and purification technologies are some of the key challenges on which studies and research in the field are focused.[13,14]

Given the importance of studying alternative raw materials to be used in fuel generation routes, the use of biogas as a precursor for obtaining green hydrogen merits to be highlighted. The dry reforming of biogas has been attracting great interest, mainly because it is a process that helps to reduce the emission of greenhouse gases,[15] since it is mainly composed of carbon dioxide (CO_2) and methane (CH_4), can act directly as an input in dry reforming.[16] On the other hand, methane dry reform (DRM) requires energetic conditions to take place, and, because of this, further investigations are needed regarding the catalyst involved in the process, mainly associated with its deactivation by coke formation and sintering.[1,17]

The reactions observed in DRM are presented by the equations shown in Table 1. Equations 3 (decomposition of methane), 4 (Boudouard), and 5 (reduction of CO), are responsible for the formation of carbon during the reaction process, which can be deposited in and on the catalyst surface leading to the deactivation of its active sites.[18] These reactions are catalyzed by acidic active sites and, the greater the acidity of the catalyst and the greater the presence of active sites with acidic characteristics, the faster the formation of coke will be.[19] From this perspective, the selection of the catalytic support is essential, since, in addition to providing mechanical and thermal stability to the material, its physicochemical characteristics are directly related to the formation of coke on the catalyst surface.[20]

Table 1. Main reactions of the processes involved in methane dry reform (DRM)

Equation	Reaction	ΔH_{298} / (kJ mol^{-1})	
1	$CH_4 + CO_2 \leftrightarrow 2CO + 2H_2$	+247,0	dry reforming of methane
2	$CO + H_2O \leftrightarrow CO_2 + H_2$	–41,0	water-gas shift
3	$CH_4 \leftrightarrow C + 2H_2$	+75,0	methane decomposition
4	$2CO \leftrightarrow C + CO_2$	–172,0	Boudouard
5	$CO + H_2 \leftrightarrow C + H_2O$	–131,0	CO reduction
6	$CO_2 + 4H_2 \leftrightarrow CH_4 + 2H_2O$	–165,00	methanation

Adapted from Alves *et al.*[1] ΔH_{298}: enthalpy change at 298 ºC.

The dispersion of the active phase on the support is another important parameter that directly influences catalyst performance and is related to catalyst deactivation by sintering.[21] According to studies carried out by Carter *et al.*[22] the catalytic activity of nickel decreases as the crystallite size increases, which, in turn, is related to the corresponding decrease in the specific area of the metal. Zhang *et al.*[23] performed an investigation of nickel catalysts dispersed on different supports and reported that the weak interaction of the support with the metal leads to a rapid catalyst deactivation due to the coalescence of metallic particles, while very strong metal-support interactions made it difficult to reduce the active phase. Hence, the choice of the support is directly related to the behavior of the active phase in the catalyst.[24]

The catalytic supports of silica, SiO_2, and Si-MCM-41, can be regarded as an alternative to DRM catalysts

because they are inert, of low acidity, and high thermal and mechanical resistance, presenting, in similar terms, very close levels of efficiency concerning Al_2O_3-based supports.[25] It is also worth mentioning that obtaining silica supports can also be associated with the processing of waste with low added value and high environmental impact,[26] for instance, on agro-industrial waste, e.g., rice husks.[27] The high content of silica in rice husk makes this residue attractive as a substitute for commercial silica in obtaining mesoporous silicate materials[28] and encouraging results can be observed in the literature[25,27,29] and in other previous works of the research group.[30-32]

In this sense, Cai *et al.*[21] evaluated the performance of catalysts with different nickel contents (3.1 to 13.2%) supported on mesoporous silica in the dry reforming reaction of methane. The authors observed that those supports, in which lower nickel contents were impregnated, showed greater maintenance of the mesoporous structure with small nickel particles highly dispersed on their surface. The catalyst with 6.7% Ni content showed promising structural properties when compared to the other catalysts (area of 484 $m^2 g^{-1}$ and pore volume of 0.57 $cm^3 g^{-1}$) and, therefore, presented a better performance in DRM, with yields of 65% for H_2 and 70% for CO in 6 h reactions, and less coke deposit on its surface. Cai *et al.*[21] obtained H_2/CO molar ratios between 0.9 and 1 for the catalysts and all of them showed good stability in 30 h reactions, with emphasis on the 6.7% Ni/SiO_2 catalyst, where a loss of only 5% conversion was observed.

Al-Fatesh *et al.*[33] evaluated the effect of Sc as a promoter in nickel catalysts supported on Si-MCM-41 and compared it with the catalyst without the addition of the promoter. The catalyst with 5% Ni supported on Si-MCM-41 evaluated by the authors showed about 63 and 71% of conversion to CH_4 and CO_2, respectively, and under conditions of 800 ºC, CH_4/CO_2 = 1, and 400 min of reaction. The authors found that the addition of low Sc contents to the catalysts (0.1 and 0.5%) resulted in the increased stability and resistance to coke deposit, but the addition of the promoter in larger quantities led to a decrease in the yield of the products.

In a previous work by the research group,[30] promising results were reported for Si-MCM-41 supported nickel catalysts applied to the dry reforming of methane. The catalyst with 20% nickel content supported on sieves synthesized from the silica source TEOS showed the best catalytic performance, producing a molar ratio H_2/CO of 1.5 and yields of H_2 and CO of 38 and 22.5%, respectively. The Si-MCM-41 supported catalysts synthesized from rice husk silica presented lower reaction performance attributed by the author to the smaller specific area obtained for the support. Furthermore, the catalysts showed excellent stabilities, with no significant loss of catalytic activity being observed within 23 h of reaction.

In this scenario, the present work represents a continuation of an extensive and in-depth study, presented in detail in a previous publication,[32] about the reaction variables that involve the preparation of the catalytic support. Thus, from the previously obtained results,[32] the relationship of the physicochemical characteristics of two different types of Si-MCM-41 supports with the nickel dispersion, in different mass percentages, 5, 10, and 20% on the surface of the catalytic support and its relationship with coke formation was investigated. Furthermore, it was possible to compare the performance of catalysts in the DRM, aiming the generation of green hydrogen as a gaseous product, evaluating stability in a 24 h reaction.

Experimental

The catalytic supports were synthesized following the methodology described in detail in Cazula *et al.*[32] and presented summarized on Supplementary Information (SI) section. The catalysts were prepared with 5, 10, and 20% (m/m) of Ni by the wet impregnation method (with an excess of solvent), using as the metal precursor salt nickel nitrate hexahydrate [$Ni(NO_3)_{2.6}H_2O$] (CAS: 13478-00-7, Neon, Suzano, Brazil).[34] After the synthesis, the materials were oven-dried for 24 h at 60 ºC and calcined in a muffle furnace at 800 ºC for 6 h. The catalysts were identified according to Table 2, in which the Ni/TEOS captions were used for catalysts in which the support was synthesized with tetraethyl orthosilicate (TEOS) as a silica precursor, and Ni/RHS for those in which the support was synthesized with rice husk ash (RHS) as a silica precursor. The RHS used for the synthesis of materials was the same used in Aguiar *et al.*[30] and its chemical composition and more information can be found in the work in question.

Table 2. Identification of synthesized catalysts

Support			
Ni content / %	5	10	20
Si-MCM-41_TEOS	5Ni/TEOS	10Ni/TEOS	20Ni/TEOS
Si-MCM-41_RHS	5Ni/RHS	10Ni/RHS	20Ni/RHS

TEOS: tetraethyl orthosilicate; RHS: rice husk ash.

The catalysts were characterized by scanning electron microscopy and energy dispersive spectroscopy (SEM/EDS) techniques, in an FEI Quanta 440 scanning electron microscope and Penta FET Precision OXFORD INSTRUMENTS (Palotina, Brazil) equipment for the EDS analysis; by transmission electron microscopy (TEM),

using an FEI Tecnai (São Carlos/SP-BR) G2 F20 200 kV FEG-TEM instrument; nitrogen physisorption (BET/BJH), in a Quantachrome (Palotina, Brazil) brand device, model Nova 2000e, in which the specific area was obtained using the Brunauer-Emmett-Teller (BET) method, using data kept in P/P_0 in the range of 0.05 to 0.3, while the pore diameter and volume were obtained by means of Barret-Joyer-Halenda (BJH) analyses; X-ray diffraction (XRD) in a Bruker diffractometer (Toledo, Brazil), model D2-PHASER, using samples in powder form, with granulometry below 106 µm, in which the readings were taken in the Bragg angle range from 0.5 to 80°, with Cu Kα radiation (λ = 1.5418 Å) and nickel filter, with a voltage of 30 kV, electrical current of 10 mA and continuous scan of 0.02 min^{-1} of the 2θ and time step of 1.0 s; Fourier transform infrared spectroscopy (FTIR), in a PerkinElmer (Toledo, Brazil) apparatus, model spectrum 65 with ATR (attenuated total reflectance) accessory, 32 scans in a reading range from 600 to 4000 cm^{-1} and spectral resolution of 0.5 cm^{-1}; temperature-programmed ammonia desorption (TPD-NH_3), in a ChemBET 3000 multipurpose system (Quantachrome Instruments) (Maringá, Brazil) equipped with a thermal conductivity detector (TCD), in which the metallic phase was reduced by 5% H_2/N_2 at 90 mL min^{-1} at 700 °C and ammonia adsorption performed at 100 °C, under a flow rate of 75 mL min^{-1} of 5% NH_3 in N_2; and temperature programmed reduction (TPR), using a home-built TPR device (Maringá, Brazil), equipped with a quartz tube in which the samples were heated from room temperature to 900 °C at a flow rate of 30 mL min^{-1} of 1.75% H_2/98.25% Ar.

The reaction tests were carried out in an experimental unit composed of a quartz fixed bed reactor at 800 °C for 24 h with a CH_4/CO_2 molar ratio equal to 1 and a flow rate of 100 mL min^{-1}. The catalysts were activated *in situ* by passing hydrogen (H_2) at 30 mL min^{-1} for 1 h, at a temperature of 800 ºC. After activation, purging was performed by passing nitrogen (N_2) through the gas line at the same flow rate for 30 min, at a temperature of 800 ºC. Analyzes of the gaseous products obtained were performed in-line in an Agilent (Rio de Janeiro, Brazil) gas chromatograph, model 6890A, equipped with a thermal conductivity detector and a Carboxen 1010 column. The coke produced was estimated by the temperature-programmed oxidation (TPO) technique, *in situ*, so that the samples were cooled to room temperature in a flow of helium gas and, subsequently, heated to 900 ºC (10 ºC min^{-1}) under a flow of 30 mL min^{-1} of a 5% O_2:He mixture; during heating, CO_2 was monitored in a Pffeifer (Rio de Janeiro, Brazil) model, Prisma Plus mass spectrometer coupled to the reactor.

Results and Discussion

In Figure 1, it can be seen the scanning micrographs for the catalysts 5Ni/TEOS (Figure 1a), 10Ni/TEOS (Figure 1b), 20Ni/TEOS (Figure 1c), 5Ni/RHS (Figure 1d),

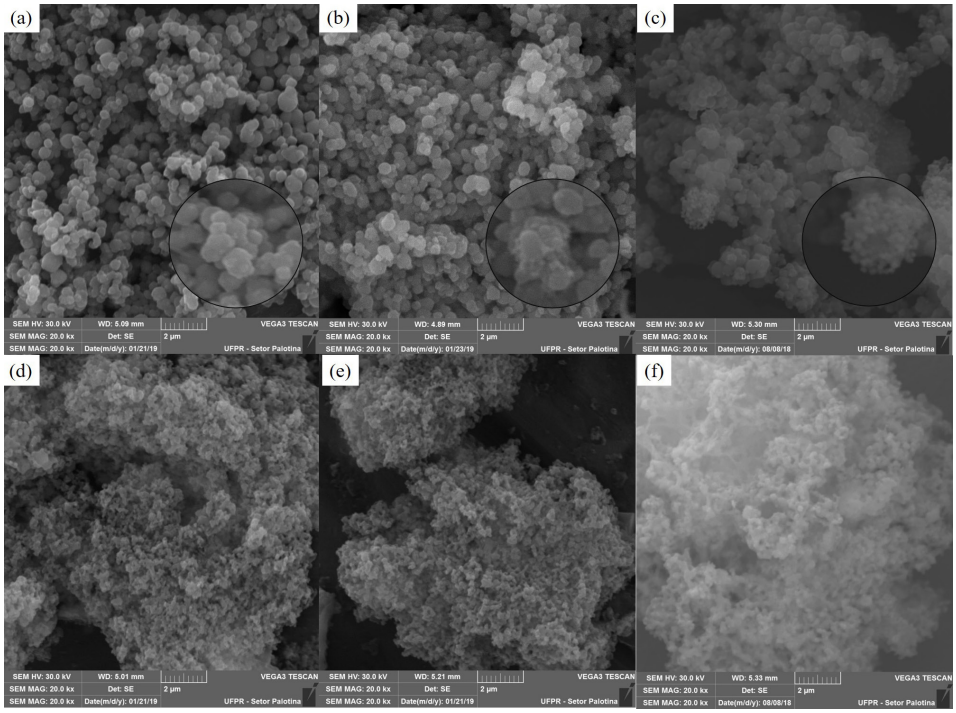

Figure 1. Micrographs (SEM) for the catalysts: 5Ni/TEOS (a), 10Ni/TEOS (b), 20Ni/TEOS (c), 5Ni/RHS (d), 10Ni/RHS (e) and 20Ni/RHS (f); magnified 20.000 times.

10Ni/RHS (Figure 1e), and 20Ni/RHS (Figure 1f). It is possible to notice that the morphology of Ni/TEOS catalysts presents itself as smooth spherical particles while, for Ni/RHS catalysts, the particles appear in the form of irregular agglomerates with a spongy appearance. The irregularity of the Ni/RHS material may be associated with the use of hydrothermal methodology and a source of residual silica in the synthesis of the precursor support.[25,35,36]

It can be observed, in the micrographs for Ni/TEOS catalysts (Figures 1a, 1b, 1c), the presence of small nickel oxide particles, located on the surfaces of the spherical particles of the support. As for the Ni/RHS catalysts (Figures 1d, 1e, 1f) these types of NiO particles are not observed on the surface of the material. The presence of segregated nickel oxide on the support surface, for Ni/TEOS catalysts, may be related to the migration of nickel from the inside of the pores to the surface of the support when calcination took place, which should not occur or occur to a lesser extent in the Ni/RHS catalysts, as observed in previous works by the group.[30]

It is possible to visually prove, through TEM micrographs (Figures 2a, 2b, 2c, for catalysts with 5, 10, and 20% Ni, respectively), the formation of nickel oxide particles on the surface of the spherical particles of the TEOS support, thus constituting the Ni/TEOS catalyst.

Regarding the TEM micrographs of Ni/RHS catalysts, it is verified that, as well as in SEM micrographs, the formation of large active phase particles on the support surface is not observed, mainly in 5Ni and 10Ni. In this case, it is noticed that nickel is more dispersed among the mesopores of the support and few or no large crystalline particles formed in the analyzed region are observed (Figures S1, S2, S3, and S4, SI section). The 20Ni/RHS catalyst merits to be emphasized for being the one that most visually resembles the TEOS catalysts, since the formation of nickel particles can be observed on the surface of the support as well as for the TEOS catalysts, as noted in Figure 2c, and with a little more attention, in Figures 1f and S5 (SI section).

The TEM micrographs show that, for RHS materials, it is possible to observe regions of greater contrast, highlighted for 5Ni/RHS (Figure 3a) and 10Ni/RHS (Figure 3b) materials, which indicate that the NiO particles are dispersed inside the support in irregular shapes (Figures S6, S7, S8 and S9, SI section). For TEOS materials, and also

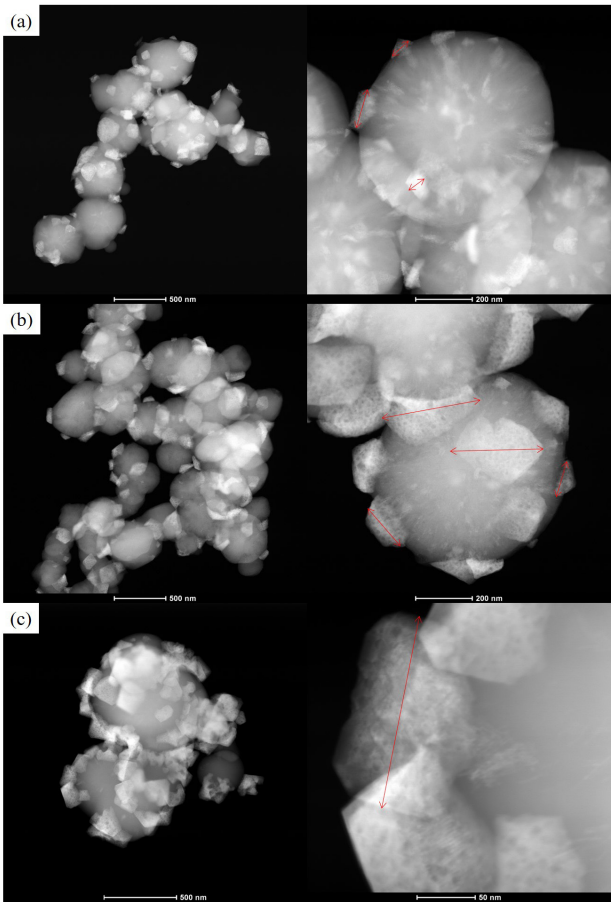

Figure 2. Micrographs (TEM) for the 5Ni/TEOS (a), 10Ni/TEOS (b), and 20Ni/TEOS (c) catalysts at different magnifications.

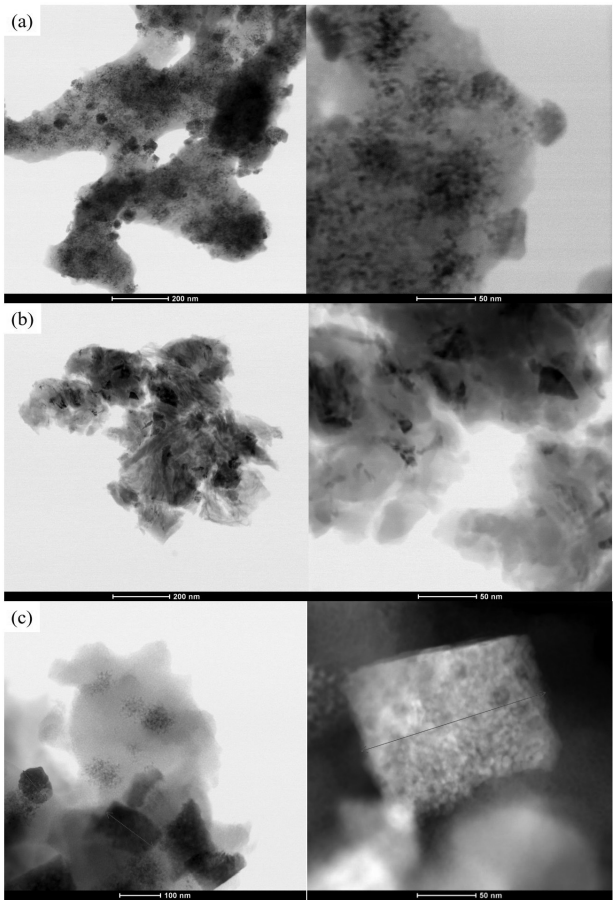

Figure 3. Micrographs (TEM) for 5Ni/RHS (a), 10Ni/RHS (b), and 20Ni/RHS (c) catalysts at distinct magnifications.

for 20Ni/RHS, nickel oxide crystals are well-formed on the surface of the support in sizes ranging from small particles of 50 nm to larger particles, with 148 nm for 20Ni/RHS and with 316 nm for 10Ni/TEOS (in red in Figures 2a, 2b and 2c, and 3c, the particles with calculated size are indicated). Thus, it can be inferred that, as the amount of nickel in the catalysts increases, the behavior of the active phase on the surface of the TEOS and RHS catalysts converges to the formation of spots with NiO concentration, in which there is the formation of crystalline particles of metal. In this context, it can be expected that the 20Ni/TEOS and 20Ni/RHS catalysts present similar behavior when compared to other structural characterization tests.

Figure 4 shows a high-resolution TEM image where is possible to observe the interface between the support and the metallic active phase. The MCM-41 mesoporous pattern clearly can be observed, and is possible to notice the change in the image when, on top, the crystalline pattern of nickel oxide is observed.

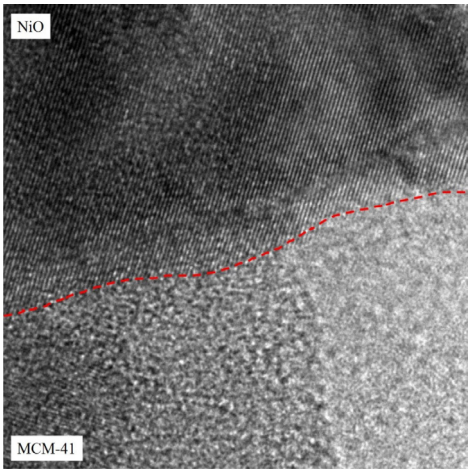

Figure 4. High-resolution TEM micrograph showing the interface between the support and the metallic active phase in the catalyst.

The evaluation of the element's content present in the catalysts, carried out using EDS analysis, are shown in Table 3. The results show that the impregnation of nickel on the supports was efficient, since the percentages of Ni obtained in the catalysts were very similar to the predicted theoretical values (5, 10, and 20%), except for the 10Ni/TEOS and 20Ni/RHS catalysts, for which the values slightly deviate. It is important to emphasize that the results may vary in composition depending on the sampling points, since the EDS technique provides semi-quantitative results.

Figure 5 shows the nitrogen adsorption and desorption isotherms for Ni/TEOS catalysts (Figures 5a, 5b, 5c) and Ni/RHS (Figures 5d, 5e, 5f), respectively. It is possible to note that the isotherm observed for the 20Ni/TEOS catalyst can be classified, according to International Union of Pure and Applied Chemistry (IUPAC)[37] as type II, characteristic of non-porous or macroporous materials. This profile may be associated with the obstruction of the entrance to the pores by the agglomeration of nickel oxide particles, corroborating the pattern observed in the micrographs, since it is evident that those catalysts with 20% nickel present more particles concentrated on the surface of the support.

The 5Ni/TEOS, 10Ni/TEOS, and 20Ni/RHS catalysts, on the other hand, presented isotherms closer to type IV and the hysteresis, evidenced for these catalysts, similar to those of type H1,[37] as it was observed for their corresponding supports precursors.[32] The type H1 hysteresis is generally associated with materials that exhibit uniform mesopores and in which the pore mouth width distribution is similar to the pore diameter distribution.[37]

The 5Ni/RHS and 10Ni/RHS catalysts also have isotherms classified as type IV, however, the identified hysteresis for these materials can be classified as type H2(b) for the material with 5% nickel and as H3 for the material with 10% nickel. The type H2(b) hysteresis is generally attributed to mesoporous materials after being subjected to high temperatures, in which there are long pores with a blocked surface, whereas type H3 hysteresis is associated with non-porous materials or materials with completely filled pores.[37]

Table 4 shows the results for a specific area, pore volume, and average pore diameter values for both catalysts. One can observe, through the presented data, that the greatest discrepancy between the textural characteristics

Table 3. Mass composition of the elements present in the catalysts, obtained by EDS, ± the standard deviation values (S)

Sample	Element mass / %		
	O	Si	Ni
5Ni/TEOS	59.12 ± 0.66	34.93 ± 0.79	5.95 ± 1.44
10Ni/TEOS	61.76 ± 0.86	30.55 ± 0.16	7.69 ± 0.70
20Ni/TEOS	50.72 ± 4.89	31.07 ± 3.51	18.21 ± 1.38
5Ni/RHS	58.83 ± 1.18	35.37 ± 1.28	5.80 ± 0.10
10Ni/RHS	56.73 ± 1.34	32.99 ± 0.47	10.29 ± 0.87
20Ni/RHS	49.42 ± 4.98	34.94 ± 3.26	15.64 ± 1.81

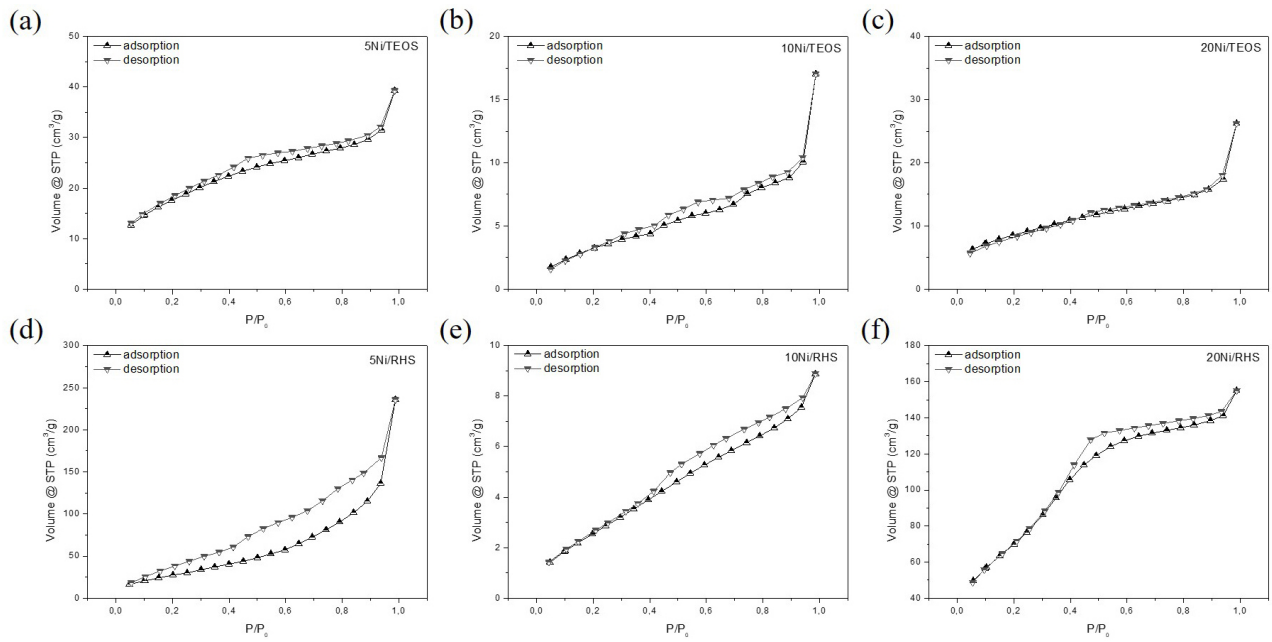

Figure 5. N_2 adsorption and desorption isotherms for the catalysts: 5Ni/TEOS (a), 10Ni/TEOS (b), 20Ni/TEOS (c), 5Ni/RHS (d), 10Ni/RHS (e) and 20NI/RHS (f).

of both catalysts occurs in the property of a specific area, so that it is possible to separate the behavior of the catalysts into two groups: the Ni/TEOS catalysts and the 10Ni/RHS catalyst, which presented similar values for the studied properties; and the 5Ni/RHS and 20Ni/RHS catalysts, in which a different profile was observed.

Table 4. Texture properties of nickel catalysts

Sample	Surface area / ($m^2 g^{-1}$)	Pore volume / ($cm^3 g^{-1}$)	Pore diameter / Å
5Ni/TEOS	63	0.03	17.7
10Ni/TEOS	13	0.02	17.7
20Ni/TEOS	30	0.03	17.7
5Ni/RHS	166	0.36	17.7
10Ni/RHS	10	0.02	17.8
20Ni/RHS	272	0.15	15.7

It can be seen that there is a difference in profile between catalysts supported on materials prepared by the two different synthesis methodologies. For Ni/TEOS catalysts, there is a behavior, in terms of specific area and pore volume values, which can be explained by the diffusion of nickel oxide particles from the interior of the pores to the surface of the support, during the calcination of material. This phenomenon is intensified for these catalysts due to the well-organized porous structure of the TEOS supports, which allows the diffusion and formation, even with only 5% of metal, of crystalline nickel oxide particles on the catalyst surface. Furthermore, the lower specific area values when compared to RHS catalysts derive both from an increase in the particle size of the catalyst and from the blocking of the entrance of the mesopores by the nickel oxide particles.[38] According to Zhang *et al.*,[23] the interaction between the silica support and the metal is weak upon comparing with other supports, such as alumina (Al_2O_3), for example, which can promote the accumulation of Ni species on the surface of the support.

For the RHS catalysts, the behavior of the investigated properties differs from that found for TEOS catalysts. In the case of the 5Ni/RHS catalyst, it is believed that nickel is concentrated inside the pores of the material, since the less uniform organization of the mesoporous network of the precursor support (characteristics of Si-MCM-41/RHS molecular sieves and how it was verified for the supports in question were studied in a previous work)[32] does not favor the diffusion of the metal to the surface. This finding can also be supported by the absence of visible NiO clusters on the surface of the support, as shown in SEM and TEM micrographs (Figures 1d and 3a). On the other hand, for the 10Ni/RHS catalyst, the similarity in the values found for the properties studied with the TEOS catalysts can also be explained considering the micrographs obtained for this material. For 10Ni/RHS, it can be noticed in Figure 3b the formation of some particles of the active phase on the surface of the catalyst, in the darker regions at the ends of the catalyst support. A possible interpretation is that, as for 5Ni/RHS, the diffusion movement of the metal from the interior of the pore towards the surface is hampered by the irregular porous structure of the support, however,

in this case, as there is a higher percentage of nickel, the pores must have been almost entirely filled with NiO, without necessarily accumulating on the surface, which corroborates with the lower specific area value when compared to other Ni/RHS catalysts.

A similar phenomenon was observed by Aguiar *et al.*,[30] in a previous work by the research group. In the case of Aguiar *et al.*,[30] a lower specific area value was observed for the catalyst with 10% nickel when compared to 20%, as it was observed in the work in question. It is believed that for 20Ni/RHS much of the Ni must be located on the surface in the oxide form, and therefore, the specific area tends to increase again, since the pore channels are more available due to the aggregation of the metal in the surface. Also, the diffusion of nickel to the surface of the support leads to the formation of crystals, as seen in the micrographs (Figures 1f and 3c), leading to a rougher surface, contributing to the higher specific area value observed.

Figure 6 shows the diffractograms for Ni/TEOS (Figures 6a, 6b, 6c) and Ni/RHS (Figures 6d, 6e, 6f) catalysts. It can be seen that all catalysts showed peaks at 37, 43, 63 and 75°, which indicate the presence of nickel oxide in the face-centered cubic phase (JCPDS47-1049), corresponding to the (111), (200), (220), and (311) planes, respectively.[21] The clear visualization of NiO diffraction peaks may be related to the weak interaction between the silica support and nickel, so that, during calcination, metal migration and oxidation by the air atmosphere occur.[23]

Comparing catalysts with 5, 10, and 20 Ni on TEOS and RHS supports, it is observed that the increase in Ni content in the catalysts is related to the increase in the intensity of the peaks identified for NiO, indicating the formation of crystals getting bigger and bigger. The intensity of the peaks, which is always higher for catalysts supported on TEOS, indicate that, in these materials, there is the formation of larger and more crystalline particles of NiO on the surface of the support,[39] which is in agreement with the interpretation that, in the case of RHS catalysts, most of the nickel is within the mesoporous network of the material, and therefore has not fully diffused to the surface.

It is possible to observe in the diffractograms of the catalysts the presence of part of the peak (2θ) close to 1.5º, but the two other peaks less than 5° of lesser intensity are not observed, referring to the hexagonal mesoporous organization of the supports, as observed for the support's precursors in a previous study.[32] The broad peak in the range of 10 to 35º, observed in all catalysts, is related to the presence of SiO_2 in the amorphous phase,[40] and was also present in the diffractograms for the precursor supports, as reported in a previous publication.[32]

The FTIR spectra of the catalysts are shown in Figure 7. One can observe, for all materials, bands referring to the symmetric and asymmetric Si–O–Si stretch around 800 and 1050 cm^{-1} respectively, related to the SiO_2 structure of the precursor support. No bands were observed at 1700 cm^{-1} and between 2900 to 3800 cm^{-1}, related to the presence of moisture in the samples, as well as no bands related to the presence of surfactant, between 2500 and 3000 cm^{-1}, proving the efficiency in the calcination of the precursor supports. In the evaluated range, no bands related to Ni–O binding were observed.[41]

The TPR profiles for the catalysts can be evaluated

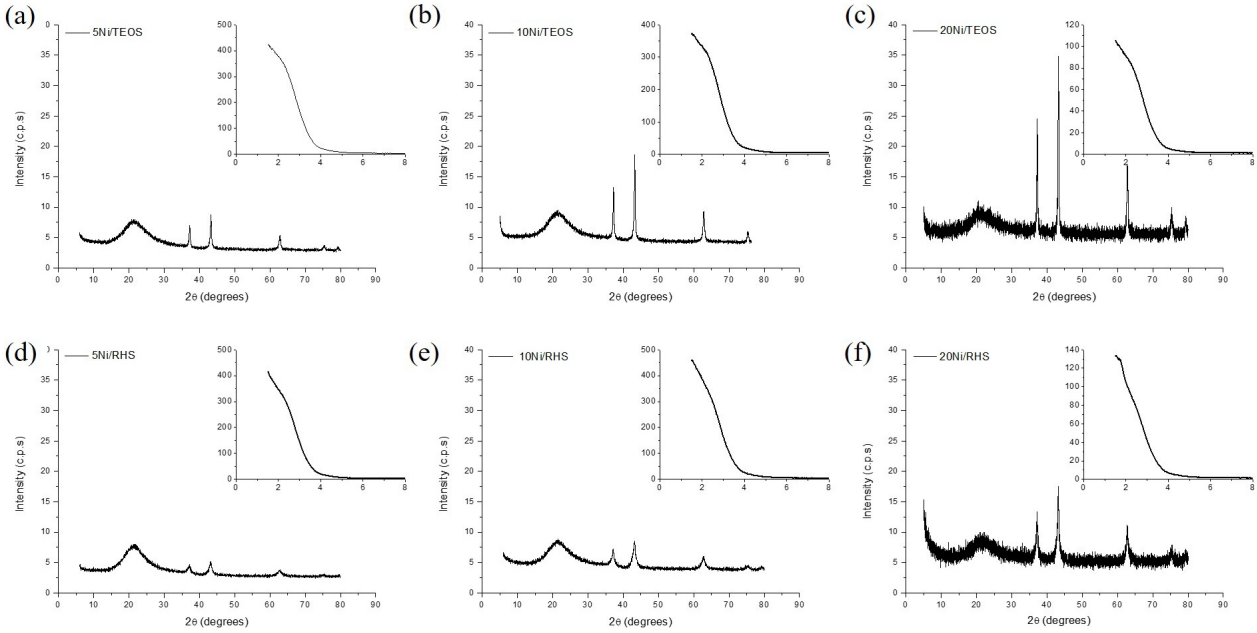

Figure 6. Diffractograms for 5Ni/TEOS (a), 10Ni/TEOS (b), 20Ni/TEOS (c), 5Ni/RHS (d), 10Ni/RHS (e) and 20Ni/RHS (f) catalysts.

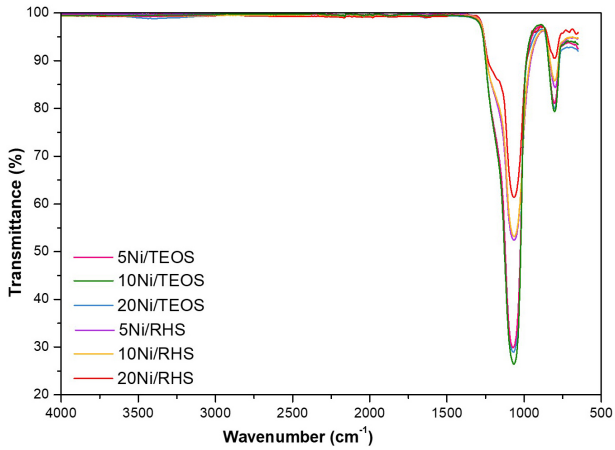

Figure 7. Infrared (FTIR-ATR) region spectra for catalysts.

in Figure 8a, for Ni/TEOS materials and Figure 8b, for Ni/RHS materials. It can be seen that, as the nickel content in the catalysts increases, the consumption of H_2 also increases. It was not possible to observe a significant reduction profile for the 5Ni/RHS and 10Ni/RHS catalysts since, for these catalysts, as seen through the structural characterization analyzes and as evidenced in the SEM micrographs (Figures 1d and 1e) and TEM (Figures 3a and 3b), there is almost no presence of solid nickel oxide on the catalyst surface.

Figure 9 shows the deconvolution of the reduction profiles, through mathematical adjustments of Gaussian functions, for samples that presented reducibility. The identified reduction peaks, as well as their respective relative areas, are shown in Table 5.

According to Figure 9, the 5Ni/TEOS sample showed four peaks of reduction at 344, 385, 437, and 532 °C. The reduction of the 10Ni/TEOS sample has some resemblance with that of the 5Ni/TEOS sample, such as a peak at 346 °C, however, this sample had five reduction events; in addition to the aforementioned, at 413, 471, 565 and 672 °C. It is verified, therefore, that the increase in the nickel oxide content from 5 to 10% in the composition of the catalysts resulted in a shift of the reductive processes to higher temperatures, which may be due to the presence of stronger NiO-support interactions, resulting from highly dispersed particles on the surface of the support. Lovell *et al.*[42] also identified this shift towards higher reduction temperatures for Ni/Si-MCM-41 samples when nickel content was increased from 2.5 to 10%. According to the authors, this shift is due to the formation of nickel hydrosilicate for samples with higher nickel content.

Four reductive events were observed in the TPR profile of the 20Ni/TEOS sample (396, 434, 489, and 650 °C). It is interesting to notice that, among all the samples in which the support was synthesized based on TEOS, this is the one with the greatest extent of reduction at temperatures below 500 °C (92.2%) when compared with 74.9% of the 5Ni/TEOS sample and 86.2% of the 10Ni/TEOS sample (Table 5). The fact that the 20Ni/TEOS sample can be more easily reduced at temperatures lower than the others may indicate the presence of larger NiO particles, which leads to less dispersion of them and, as a consequence, less interaction with the support. Similar results were reported by Aguiar *et al.*,[30] who investigated nickel oxide particles deposited on Si-MCM-41 supports, synthesized from the TEOS precursor. According to the authors, lower concentrations of NiO favor the dispersion of particles and, consequently, their reducibility. Higher contents tend to reduce the dispersion of particles, resulting in a decrease in their reducibility. The existence of multiple reduction peaks in the TPR profiles is attributed, according to the authors, to the existence of particles with different degrees of interaction with the support; the greater the NiO-support interaction, the greater the difficulty for its reduction and, consequently, higher temperatures are necessary to reduce the oxide particles, which allows us to infer that the dispersion of NiO over the support surface in the present work is considerably heterogeneous. Cai *et al.*[21] investigated the reducibility of

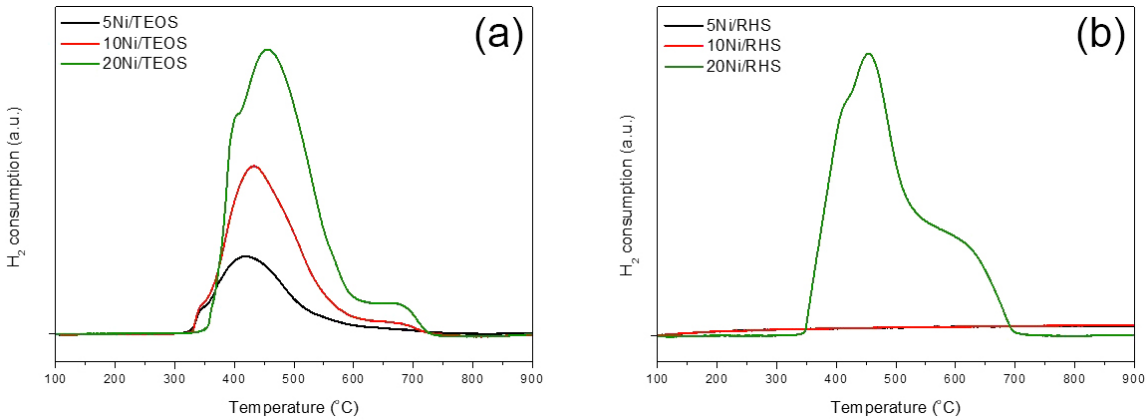

Figure 8. Temperature-programmed reduction profiles for Ni/TEOS (a) and Ni/RHS (b) catalysts.

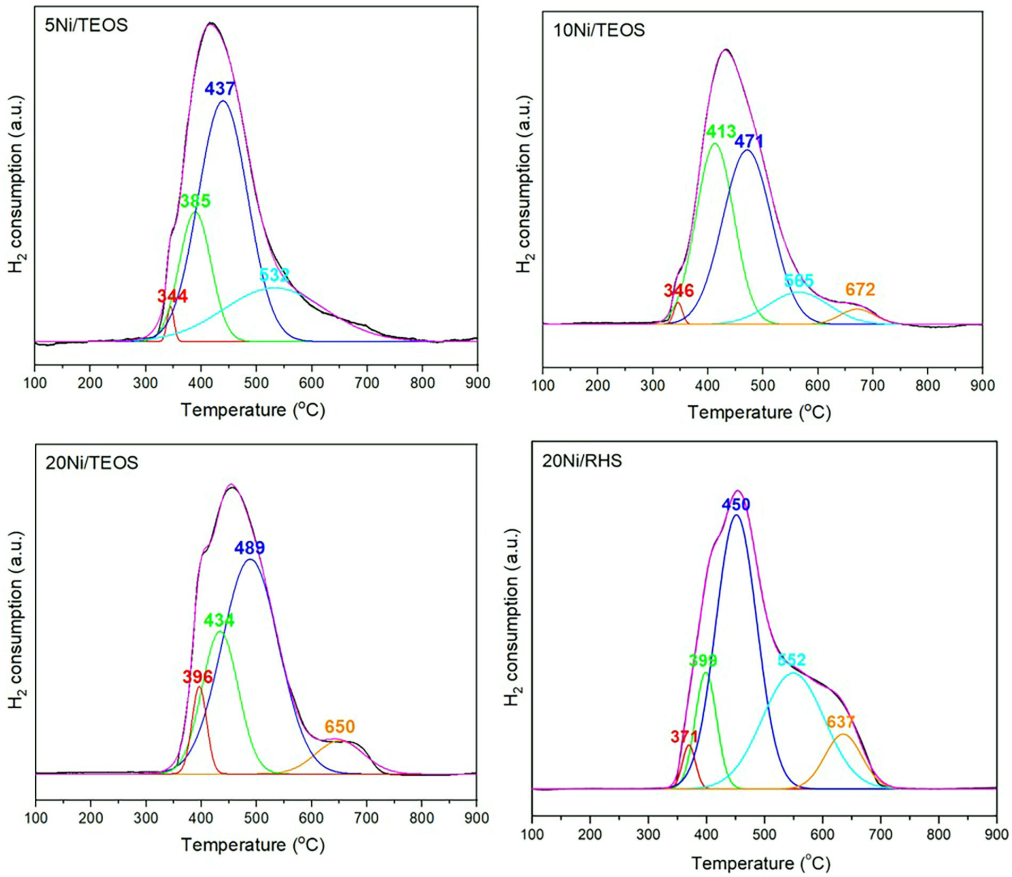

Figure 9. Deconvolution of TPR profiles through Gaussian fits: in black, observed data; in pink, mathematical model; in red, green, blue, cyan, and orange, individual reduction peaks.

Table 5. Reduction temperatures (T) and relative areas (A) of reductive events

Sample	Peak 1		Peak 2		Peak 3		Peak 4		Peak 5	
	T / °C	A / %	T / °C	A / %	T / °C	A / %	T / °C	A / %	T / °C	A / %
5Ni/TEOS	344	1,1	385	18,9	437	54,9	532	25,1	–	-
10Ni/TEOS	346	1,0	413	37,9	471	47,3	565	10,8	672	3,0
20Ni/TEOS	396	6,3	434	25,5	489	60,4	650	7,8	–	–
20Ni/RHS	371	2,4	399	10,6	450	47,9	552	30,6	637	8,5

NiO particles anchored in mesoporous silica. The authors reported the presence of reduction peaks at relatively low temperatures (287-308 °C), which were attributed to the reduction of isolated NiO particles, i.e., not anchored to silica, while the reductive processes of the anchored particles started at temperatures in the range of 450-470 °C. As in the present work, there was no identification of relevant reductive processes at temperatures below 344 °C, which allows us to infer that the presence of isolated NiO particles is insignificant, which reveals that the nanoparticle deposition methodology used in this work was adequate. Lovell *et al.*[42] also observed reduction peaks for Ni/MCM-41 samples in the range of 500-580 °C, which the authors associated with the reduction of very small NiO particles with high interaction with the support while the TPR profile of pure NiO peaks at 420 °C.

The 20 Ni/RHS sample, in turn, presented five reduction peaks centered at 371, 399, 450, 552, and 637 °C. Comparing the reduction profiles of the samples with 20% nickel, one can notice the considerable differences, which allows us to infer that the support exerts an influence on the reduction of NiO particles on its surface. The fact that the TPR profile of the 20Ni/RHS sample presents more significant reduction events at temperatures above 500 °C when compared to the 20Ni/TEOS sample reveals the greater difficulty in reducing a portion of NiO on its surface, which corroborates the findings based on the other characterization analyses, in which the location of

NiO particles inside the pores of the RHS support was evidenced, whose access by gas molecules is difficult, resulting in the need for higher temperatures for its reduction in respect to NiO particles found on the external surface of the supports originated from the use of the TEOS precursor. According to Aguiar *et al.*,[30] the higher reduction temperatures for samples whose support was synthesized from RHS compared to those originated from TEOS is due to the greater metal-support interaction.

In this context, it can be concluded that both the NiO content and the silica source used for the support synthesis are variables that affect the catalyst reducibility.

The graph showing the TPD-NH_3 profiles for the catalysts is depicted in Figures 10a and 10b, for the Ni/TEOS and Ni/RHS catalysts, respectively. It is observed that the catalysts had very low acidity since the desorption peaks are of low intensity. For RHS catalysts, it is noted that the acidity is even lower, since, especially in the cases of 5Ni/RHS and 10Ni/RHS, the presence of nickel on the surface of the supports is almost non-existent. It is worth mentioning that the increase or decrease in the baseline is derived from the heating rate.

Thus, considering the results of the structural and morphological characterization analysis of the catalysts, it is expected that the materials, especially the RHS, since they present low acidity, due to the nickel disposition towards the interior of the support, directly collaborate in the low formation of solid carbon during reaction tests,[43,44] when compared to works available in the literature.[21,25,30,33] At the same time, it is believed that, for TEOS catalysts, the disposition of active phase particle agglomerates on the catalyst surface contributes to greater efficiency of these catalysts about reaction tests, since the surface active sites, as they are more available, are sufficient to convert the reagents into products, thus dispensing those that would eventually be inside the pores.

The catalysts were applied in the methane dry reforming reaction and the results of: CH_4 and CO_2 conversion and product selectivity are shown in Figure 11; the results of the molar fraction of the gaseous reactants and products, in Figure 12; the H_2:CO molar ratio for the reaction assays, in Figure 13; and the molar fraction results for water, in Figure 14.

From the results of the reaction tests, it is possible to observe that the catalysts 5Ni/TEOS, 5Ni/RHS, and 10Ni/RHS presented a more unstable and irregular behavior upon being compared to other materials. For the 5Ni/TEOS catalyst, it is possible to observe through the results of conversion and selectivity and molar fraction, that, although slightly unstable, the material is still selective since during the 24 h of reaction, the molar fractions of H_2 and CO are, on average equal to 32 and 39%, respectively.

The 5Ni/RHS and 10Ni/RHS catalysts were not selective when applied to the DRM, since it is possible to notice in the results of both conversion and selectivity and for the molar fraction, that the percentages of CH_4 and CO are higher than the of H_2 and CO_2. This behavior is due to the occurrence of parallel reactions to the methane dry reform. These reactions should, in theory, occur in little or no quantity, however, the combination of these two catalysts with the reaction conditions employed led to the favoring of other than the dry reforming reaction, the methanation reaction (equation 6, Table 1).

For the 10NiTEOS, 20Ni/TEOS, and 20Ni/RHS catalysts a very similar behavior was observed. The 10Ni/TEOS and 20Ni/TEOS catalysts presented very similar profiles, showing themselves to be stable and selective in 24 h of reaction. The 10Ni/TEOS catalyst had conversion values for CH_4 and CO_2 equal to 76 and 86% while the 20Ni/TEOS had conversions equal to 73 and 80% for CH_4 and CO_2, respectively. For the 10Ni/TEOS catalyst the selectivity results for H_2 and CO were equal to 45 and 49% while for the 20Ni/TEOS catalyst they were equal to 47 and 49%, respectively. The 20Ni/RHS catalyst was also stable and selective for 24 h of reaction. The conversion values for CH_4 and CO_2 were equal to 65 and 74% and for selectivity

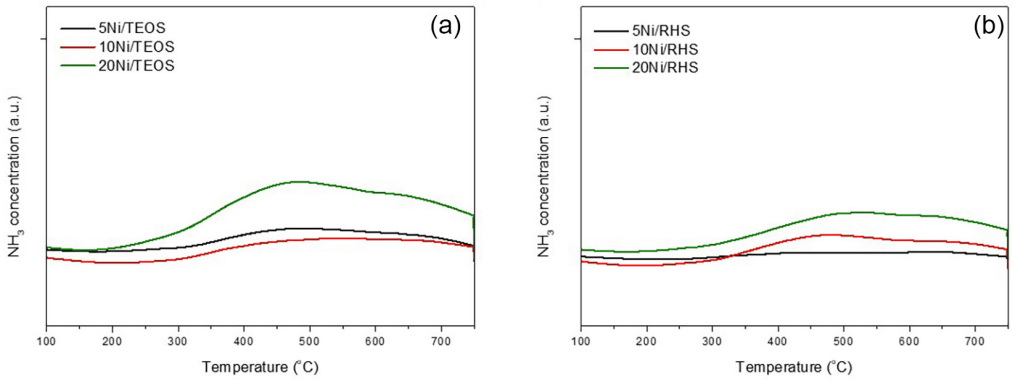

Figure 10. TPD-NH_3 profiles for Ni/TEOS (a) and Ni/RHS (b) catalysts.

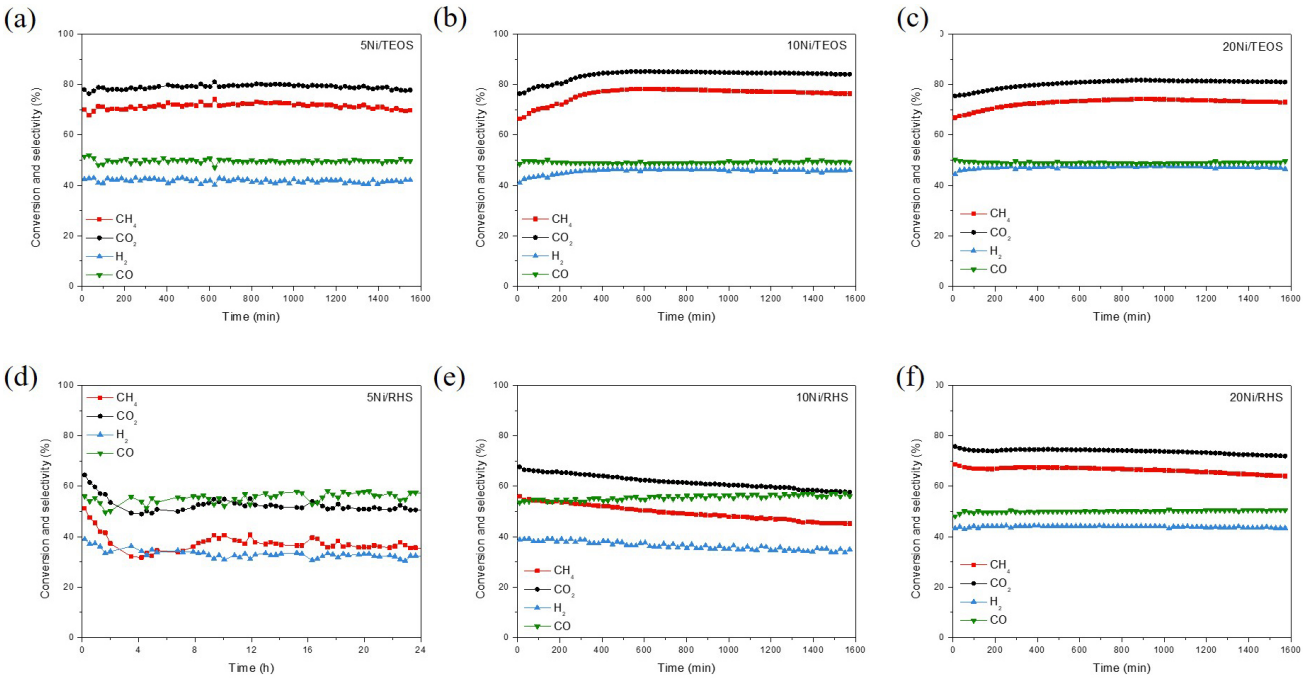

Figure 11. CH_4 and CO_2 conversion results and selectivity for H_2 and CO for the catalysts: 5Ni/TEOS (a), 10Ni/TEOS (b), 20Ni/TEOS (c), 5Ni/RHS (d), 10Ni/RHS (e), and 20Ni/RHS (f).

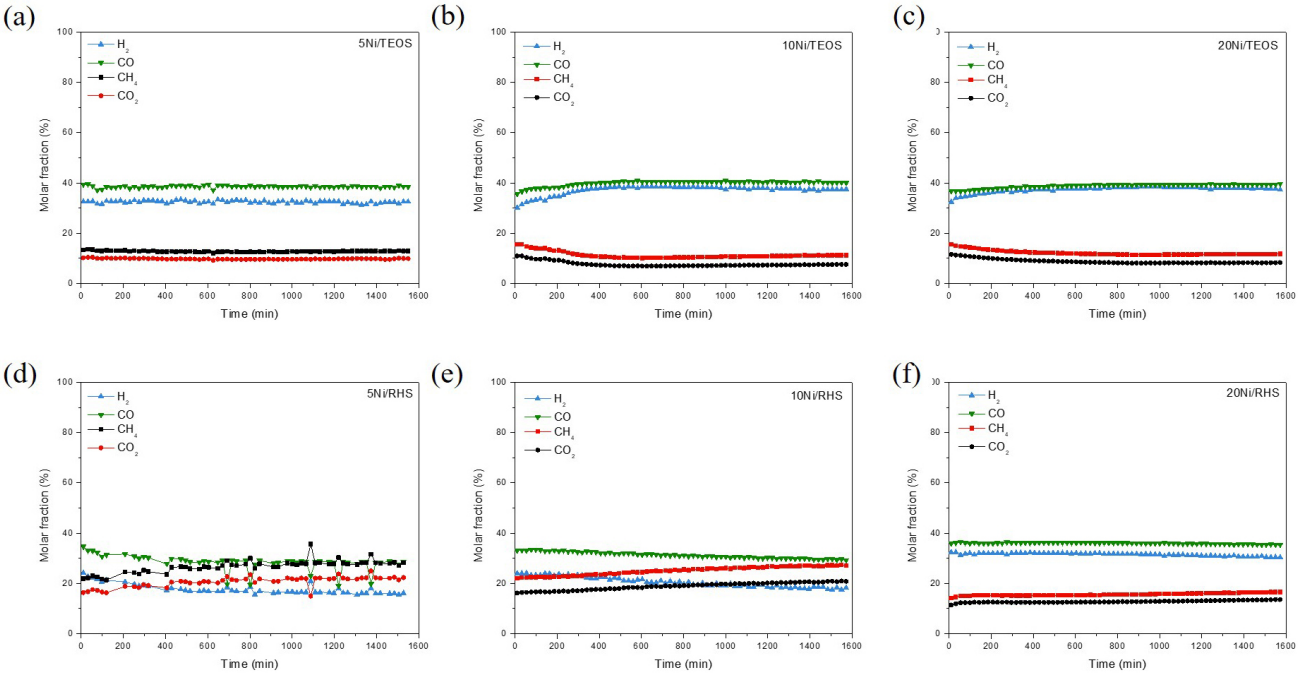

Figure 12. Molar fraction for the catalysts: 5Ni/TEOS (a), 10Ni/TEOS (b), 20Ni/TEOS (c), 5Ni/RHS (d), 10Ni/RHS (e) and 20Ni/RHS (f).

of H_2 and CO equal to 43 and 50%, respectively. The values obtained for molar fraction are also very similar for these same highlighted catalysts. The 5Ni/TEOS catalyst was the one that resulted in minimally inferior results when being compared to 10Ni/TEOS and 20Ni/TEOS, presenting molar fractions for CH_4 and CO_2, equal to 12 and 9% while the molar fractions for the products were 37% for H_2 and 38% for CO.

All catalysts, except 5Ni/RHS and 10Ni/RHS, presented molar ratio H_2:CO ranging between 0.80 and 0.98, as can be seen in Figure 13, indicating that the dry reforming reaction of methane (equation 1, Table 1) was favored. The 20Ni/TEOS catalyst stands out, with a molar ratio closer to 1 (0.98). For the 5Ni/RHS and 10Ni/RHS catalysts, in which there was a higher occurrence of parallel

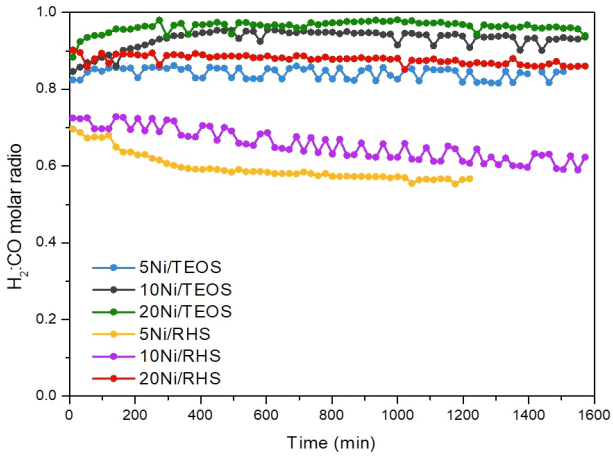

Figure 13. Molar ratio of H_2:CO for the catalysts.

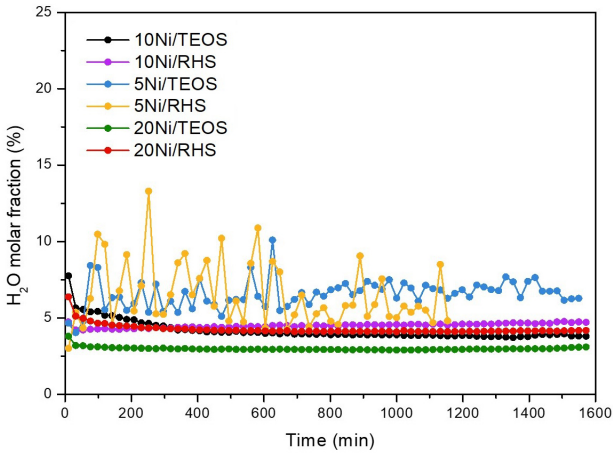

Figure 14. Molar fraction of water for reaction tests.

secondary reactions, this profile may be associated with the distribution of the active phase on the catalyst surface. In these cases, as observed in SEM and TEM micrographs, nickel tends to be in very little quantity on the surface of the catalysts, making the active phase less available for the reforming reaction.[33]

Note that, for all cases and highlighted for the catalysts 10NiTEOS, 20Ni/TEOS, and 20Ni/RHS, the molar fraction of CO is slightly higher than that of H_2. This is due to the probable occurrence of parallel reactions, already mentioned above, such as the water-gas shift reaction (equation 2, Table 1), CO reduction reaction (equation 5, Table 1) and methanation reaction (equation 6, Table 1), in which the H_2 product of the reforming reaction acts as a reactant, generating secondary products such as water.[45] Figure 14 shows the formation of water in the reaction medium, derived from the possible occurrence of the aforementioned reactions, which is greater for the 5Ni/TEOS and 5Ni/RHS catalysts.

It is necessary to emphasize that, as expected, the TEOS catalysts showed high efficiency in reactional tests, highlighting the excellent stability in 24 h of 10Ni/TEOS and 20Ni/TEOS reaction. The excellent performance of these materials is related to the disposition of the active phase on the catalyst surface. Thus, active sites widely available across the surface of catalysts lead to the conversion of reactants to products so that the reaction takes place superficially. As for the RHS catalysts, the highlight is the catalyst with higher nickel content, 20Ni/RHS, for which the performance against DRM was very similar to the 10Ni/TEOS and 20Ni/TEOS catalysts.

In terms of coke formation, it can be observed, through Figure 15 obtained by the TPO analysis, peaks between 600 and 750 ºC referring to the deposit of solid carbon on the surface of the catalysts. It is possible to differentiate peaks in different regions for both catalysts, so that, for the 10Ni/TEOS and 20Ni/TEOS catalysts, the coke oxidation peak appears around 700 °C and can be attributed to polymeric carbon not structurally organized.[46] For 5Ni/TEOS, 5Ni/RHS, and 20Ni/RHS, the peak appears at a lower temperature, around 600 ºC, and is related to the formation of carbon in the form of nanotubes.[47] It is also noteworthy that, for the 5Ni/RHS catalyst, as well as for the 10Ni/RHS catalyst, in which no carbon reduction profile was observed, the occurrence of carbon deposit on the catalyst surface was not significant.

The morphology of the solid carbon formed may be directly related to the region of the catalyst in which the coke was formed and the amorphous carbon observed on the surface of the 10Ni/TEOS and 20Ni/TEOS catalysts

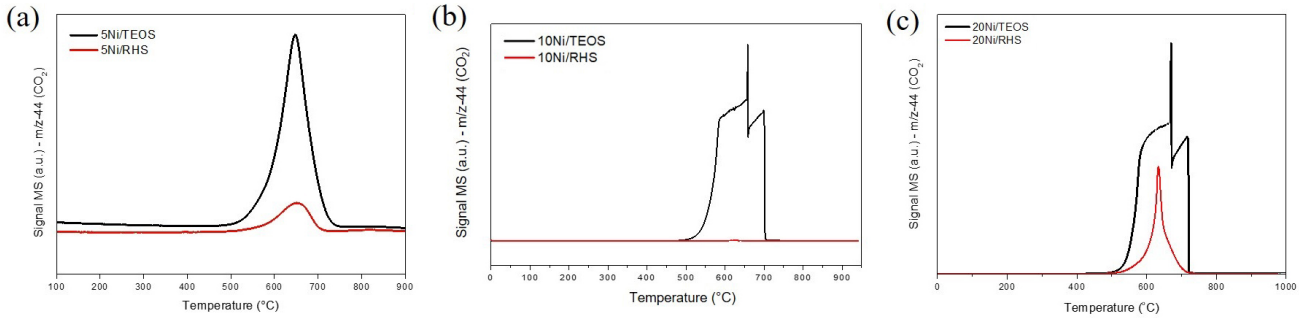

Figure 15. TPO results for the catalysts: 5Ni/TEOS and 5Ni/RHS (a), 10Ni/TEOS and 10Ni/RHS (b), and 20Ni/TEOS and 20Ni/RHS (c).

was probably formed without access to the pores of the precursor support, leading to a relationship with the fact that the reaction occurs on the surface, for these catalysts, since most of the active sites are available on the surface of the catalyst. In the 5Ni/TEOS, 5Ni/RHS, and 20Ni/RHS catalyst, the occurrence of carbon in the form of nanotubes may be associated with its formation in pore mouth regions, since, in these catalysts, there is less or no nickel agglomerate on the catalyst surface, leading to active sites for the reactions to occur, located inside the pores.

The peak intensity in the TPO curves is directly correlated with the amount of coke deposited on the catalysts. The values for solid carbon formed are shown in Table 6, in which the values in milligrams of carbon *per* grams of catalyst for each hour of reaction are presented, and the values in grams of carbon in the total 24 h of reaction testing, in the first and second column respectively.

Table 6. Quantification of solid carbon formed in reaction tests

Sample	Carbon formed / ($mg_C\ g_{cat}^{-1}\ h^{-1}$)	Carbon formed in 24 h of reaction / g
5Ni/TEOS	5.0	0.006
10Ni/TEOS	45.9	0.055
20Ni/TEOS	47.8	0.046
5Ni/RHS	1.1	0.001
10Ni/RHS	0.12	0.000
20Ni/RHS	10.3	0.010

The coke formation is associated with the occurrence of parallel reactions that generate solid carbon as a reaction product: the methane decomposition reaction (equation 3, Table 1); Boudouard reaction (equation 4, Table 1); and CO reduction reaction (equation 5, Table 1).[48] It is observed, from the data shown in Table 6, that the 20Ni/TEOS catalyst was for which the formation of coke was higher and greater emphasis is given to the RHS catalysts, which presented very similar values to each other and significantly lower. For 5Ni/RHS and 10Ni/RHS, coke formation is lower, but it is important to associate that the catalytic activity for these materials was lower, since the amount of nickel available on the surface is not enough for a good performance of the DRM. On the other hand, the 20Ni/RHS catalyst presented, in addition to stability and efficiency in reactional tests, significantly lower coke formation.

Conclusions

Through the results presented, it was possible to note that the morphology of the support is closely related to the dispersion of nickel in the catalyst. Thus, the main difference noted between the TEOS and RHS catalysts was related to the diffusion of nickel from the interior of the pores towards the surface of the catalyst. The diffusion phenomenon is facilitated in TEOS supports due to the regular and uniform morphology of the mesopores network of these materials. Therefore, it is observed the formation of large particles of active phase on the surface of the support, leading to better performance of these catalysts against DRM when compared to RHS catalysts.

For the 20Ni/RHS catalyst, it is observed the formation of Ni agglomerates on the surface of the support due to the increase in the nickel content. It should be noted that, for RHS catalysts, coke formation was significantly lower when compared to TEOS catalysts. This behavior is precisely linked to the lower acidity observed for these catalysts.

It is needed to emphasize that the 20Ni/TEOS catalyst stands out compared to other TEOS catalysts in terms of the results for the reaction tests. Its superior performance may be directly associated with its greater ease of reduction at temperatures lower than 5Ni/TEOS and 10Ni/TEOS, since it presents more agglomerated active phase particles, i.e., forming clusters on the surface of the catalytic support. Hence, it is likely that the active phase has been completely or most efficiently reduced, which contributes to its better performance against DRM.

From this perspective, the catalysts evaluated in this work, especially the 20Ni/RHS catalyst, present very interesting performances, being stable, selective, and active, when compared to works available in the literature[21,33,49,50] and previous work by the research group.[30] The differences between the performance of catalysts prepared from supports synthesized from two different synthesis methodologies and silica sources proved to be subtle, in the case of 20Ni/TEOS and 20Ni/RHS, and it may be possible to obtain promising results from catalysts supported on materials based on alternative sources of silica, as in this case, rice husk ash silica, especially when it comes to the formation of coke on the surface of the catalyst.

Supplementary Information

Supplementary information data (experimental and quantitative area EDS, differential item functioning (DIF) analysis and EDX results for the catalysts, obtained through TEM analysis) is available free of charge at http://jbcs.sbq.org.br as PFD file.

Acknowledgments

The authors thank the National Institute of Technology (INT), International Center of Renewable

Energy (CIBiogás), and the Paraná Energy Company (Copel). This Project is part of the P&D ANEEL - PD-06491-0287/2012 and it was partially financed by ANEEL/COPEL-Brazil (PD 2866-0470-2017).

Author Contributions

Bárbara B. Cazula were responsible for conceptualization, data curation, investigation, validation, visualization, writing original draft, writing-review and editing; Renata O. da Fonseca for data curation, investigation; André Luiz A. Marinho for data curation, investigation; Fábio B. Noronha for resources, writing-review and editing; Pedro Augusto Arroyo for resources; Carlos I. Yamamoto for resources; Rodrigo Brackmann for data curation, writing-review and editing; Helton José Alves for conceptualization, formal analysis funding acquisition, project administration, resources, writing-review and editing.

References

1. Alves, H. J.; Júnior, C. B.; Niklevicz, R. R.; Frigo, E. P.; Frigo, M. S.; Coimbra-Araújo, C. H.; *Int. J. Hydrogen Energy* **2013**, *38*, 5215. [Cropssref]
2. Zhang, L.; Wu, W.; Zhang, Y.; Zhou, X.; *Catal. Today* **2018**, *318*, 39. [Crossref]
3. Marchese, M.; Buffo, G.; Santarelli, M.; Lanzini, A.; *J. CO_2 Util.* **2021**, *46*, 101487. [Crossref]
4. Dalpaz, R.; Konrad, O.; Cyrne, C. C. S.; Barzotto, H. P.; Hasan, C.; Guerini Filho, M.; *Sustainable Energy Technol. Assessments* **2020**, *40*, 100774. [Crossref]
5. Romero, H. I.; Vega, C.; Feijoó, V.; Villacreses, D.; Sarmiento, C.; *Energy Rep.* **2020**, *6*, 351. [Crossref]
6. IEA, *Decarbonising Industry with Green Hydrogen*, https://www.iea.org/articles/decarbonising-industry-with-green-hydrogen, accessed in July 2023.
7. Li, L.; Chen, J.; Zhang, Q.; Yang, Z.; Sun, Y.; Zou, G.; *J. Cleaner Prod.* **2020**, *274*, 122256. [Crossref]
8. Abdalla, A. M.; Hossain, S.; Nisfindy, O. B.; Azad, A. T.; Dawood, M.; Azad, A. K.; *Energy Convers. Manage.* **2018**, *165*, 602. [Crossref]
9. Veras, T. S.; Mozer, T. S.; dos Santos, D. C. R. M.; César, A. S.; *Int. J. Energy Res.* **2017**, *42*, 2018. [Crossref]
10. IEA, *Hydrogen*, https://www.iea.org/fuels-and-technologies/hydrogen, accessed in July 2023.
11. The Future of Hydrogen, https://www.iea.org/reports/the-future-of-hydrogen, accessed in August 2023.
12. Sazali, N.; *Int. J. Hydrogen Energy* **2020**, *45*, 18753. [Crossref]
13. Dawood, F.; Anda, M.; Shafiullah, G. M.; *Int. J. Hydrogen Energy* **2020**, *45*, 3847. [Crossref]
14. Fan, Z.; Weng, W.; Zhou, J.; Gu, D.; Xiao, W.; *J. Energy Chem.* **2020**, *58*, 415. [Crossref]
15. Iulianelli, A.; Manisco, M.; Le Valant, A.; Epron, F.; Colpan, C. O.; Esposito, E.; Jansen, J. C.; Gensini, M.; Caravella, A.; *Int. J. Hydrogen Energy* **2021**, *46*, 29183. [Crossref]
16. Guilhaume, N.; Bianchi, D.; Wandawa, R. A.; Yin, W.; Schuurman, Y.; *Catal. Today* **2021**, *375*, 282. [Crossref]
17. Dobladez, J. A. D.; Ismael, V. Á. M.; Torrellas, S. A.; Larriba, M.; Brea, P.; *Int. J. Hydrogen Energy* **2020**, [Crossref]
18. Abdel, N.; Aramouni, K.; Touma, J. G.; Tarboush, B. A.; Zeaiter, J.; Ahmad, M. N.; *Renew. Sustainable Energy Rev.* **2018**, *82*, 2570. [Crossref]
19. Jang, W.; Shim, J.; Kim, H.; Yoo, S.; Roh, H.; *Catal. Today* **2019**, *324*, 15. [Crossref]
20. Chen, F.; Jiang, X.; Zhang, L.; Lang, R.; Qiao, B.; *Chinese J. Catal.* **2018**, *39*, 893. [Crossref]
21. Cai, W.; Ye, L.; Zhang, L.; Ren, Y.; Yue, B.; Chen, X.; He, H.; *Materials* **2014**, *7*, 2340. [Crossref]
22. Carter, J. L.; Cusumano, J. A.; Sinfelt, J. H.; *J. Phys. Chem. A* **1966**, *70*, 2257. [Crossref]
23. Zhang, R.; Xia, G.; Li, M.; Wu, Y.; Nie, H.; Li, D.; *J Fuel Chem. Technol.* **2015**, *43*, 1359. [Crossref]
24. Das, S.; Ashok, J.; Bian, Z.; Dewangan, N.; Wai, M. H.; Du, Y.; Borgna, A.; Hidajat, K.; Kawi, S.; *Appl. Catal., B* **2018**, *230*, 220. [Crossref]
25. Duczinski, R.; Bernard, F.; Rojas, M.; Duarte, E.; Chaban, V.; Vecchia, F. D.; Menezes, S.; Einloft, S.; *J. Nat. Gas Sci. Eng.* **2018**, *54*, 54. [Crossref]
26. Ma, Y.; Chen, H.; Shi, Y.; Yuan, S.; *Mater. Res. Bull.* **2016**, *77*, 258. [Crossref]
27. Panek, R.; Wdowin, M.; Franus, W.; Czarna, D.; Stevens, L. A.; Deng, H.; Liu, J.; Sun, C.; Liu, H.; Snape, C. E.; *J. CO2 Util.* **2017**, *22*, 81. [Crossref]
28. Steven, S.; Restiawaty, E.; Bindar, Y.; *Renew. Sustainable Energy Rev.* **2021**, *149*, 111329. [Crossref]
29. Mobarak, M.; Mohamed, E. A.; Selim, A. Q.; Eissa, M. F.; Seliem, M. K.; *J. Mol. Liq.* **2019**, *273*, 68. [Crossref]
30. Aguiar, M.; Cazula, B. B.; Colpini, L. M. S.; Borba, C. E.; da Silva, F. A.; Noronha, F. B.; Alves, H. J.; *Int. J. Hydrogen Energy* **2019**, *44*, 32003. [Crossref]
31. Cazula, B. B.; da Fonseca, R. O.; Noronha, F. B.; Alves, H. J.; *Rev. Matéria* **2021**, *26*, 1. [Crossref]
32. Cazula, B. B.; Oliveira, L. G.; Machado, B.; Alves, H. J.; *Mater. Chem. Phys.* **2021**, *266*, 124553. [Crossref]
33. Al-fatesh, A. S.; Atia, H.; Abu-dahrieh, J. K.; Ibrahim, A. A.; Eckelt, R.; Armbruster, U.; Abasaeed, A. E.; Fakeeha, A. H.; *Int. J. Hydrogen Energy* **2019**, *44*, 20770. [Crossref]
34. Mezalira, D. Z.: *Preparação e Caracterização de Materiais com Propriedades Catalíticas para a Obtenção de Hidrogênio e Carbono Nanoestruturado a partir da Decomposição de Etanol e do Glicerol*; PhD Thesis, Universidade Federal de Santa Catarina, Florianópolis, 2011. [Link] accessed in July 2023

35. Cheng, H.; Feng, S.; Tao, W.; Lu, X.; Yao, W.; Li, G.; Zhou, Z.; *Int. J. Hydrogen Energy* **2014**, *39*, 12604. [Crossref]
36. Kresge, C. T.; Leonowicz, M. E.; Roth, W. J.; Vartuli, J. C.; Beck, J. S.; *Nature* **1992**, *359*, 710. [Crossref]
37. Thommes, M.; Kaneko, K.; Neimark, A. V.; Olivier, J. P.; Rodriguez-Reinoso, F.; Rouquerol, J.; Sing, K. S. W.; *Pure Appl. Chem.* **2015**, *87*, 1051. [Crossref]
38. Salam, M. A.; Abdullah, B.; *Mater. Chem. Phys.* **2017**, *188*, 18. [Crossref]
39. Zanoteli, K.; Freitas, J. C. C.; da Silva, P. R. N.; *Quim. Nova* **2014**, *37*, 1657. [Crossref]
40. Mor, S.; Manchanda, C. K.; Kansal, S. K.; Ravindra, K.; *J. Cleaner Prod.* **2017**, *143*, 1284. [Crossref]
41. Silva, A. S.; da Silva, F. L. H.; Carvalho, M. W. N. C.; Pereira, K. R. O.; *Quim. Nova* **2012**, *35*, 683. [Crossref]
42. Lovell, E.; Jiang, Y.; Scott, J.; Wang, F.; Suhardja, Y.; Chen, M.; Huang, J.; Amal, R.; *Appl. Catal., A* **2014**, *473*, 51. [Crossref]
43. Wu, L.; Xie, X.; Ren, H.; Gao, X.; *Mater. Today Proc.* **2021**, *42*, 153. [Crossref]
44. Arora, S.; Prasad, R.; *RSC Adv.* **2016**, *6*, 108668. [Crossref]
45. Abdulrasheed, A.; Jalil, A. A.; Gambo, Y.; Ibrahim, M.; Hambali, H. U.; Hamid, M. Y. S.; *Renew. Sustainable Energy Rev.* **2019**, *108*, 175. [Crossref]
46. Ochoa, A.; Arregi, A.; Amutio, M.; Gayubo, A. G.; Olazar, M.; Bilbao, J.; Castaño, P.; *Appl. Catal., B* **2018**, *233*, 289. [Crossref]
47. Chen, K.; Xue, Z.; Liu, H.; Guo, A.; Wang, Z.; *Fuel* **2013**, *113*, 274. [Crossref]
48. Yabe, T.; Sekine, Y.; *Fuel Process. Technol.* **2018**, *181*, 187. [Crossref]
49. Chen, X.; Jiang, J.; Tian, S.; Li, K.; *Catal. Sci. Technol.* **2015**, *5*, 860. [Crossref]
50. Tian, J.; Li, H.; Zeng, X.; Wang, Z.; Huang, J.; Zhao, C.; *Chinese J. Catal.* **2019**, *40*, 1395. [Crossref]

Submitted: April 3, 2023
Published online: August 8, 2023